An Integrated Compliant Balloon Ultrasound Catheter for Intravascular Strain Imaging

Charles D. Choi, *Senior Member, IEEE*, Andrei R. Skovoroda, Stanislav Y. Emelianov, *Member, IEEE*, and Matthew O'Donnell, *Fellow, IEEE*

***Abstract*—An integrated compliant balloon ultrasound catheter was developed to allow greater deformations in strain imaging with intravascular ultrasound. A 64-element circumferential array was placed inside a compliant silicone balloon catheter to capture real-time, phase-sensitive radio frequency (RF) data during deformation experiments. Strains over 40% could be applied to normal arterial wall tissue with intracatheter pressures as low as 200 kPa (2 atm). Strain images of a hard-soft rubber phantom, thrombus, and fibrotic plaque were produced using the integrated balloon ultrasound catheter. Results show that this catheter can apply large deformations at low pressures and image various vascular pathologies ex vivo. Potentially, it can serve as a multifunctional, intravascular therapeutic device to guide angioplasty and stent deployment.**

I. Introduction

An estimated 926,000 percutaneous transluminal coronary angioplasty (PTCA) and stent procedures were performed in the United States in 1998. The number of PTCAs increased 248% between 1987 and 1998 [1]. Indeed, there are now over a million PTCA procedures performed annually in the United States alone.

Due to the increasing number of PTCA procedures, there has been growing interest in measuring and understanding mechanical properties of arterial tissues and pathologies to better treat vascular diseases [2]–[12]. Intravascular ultrasound can serve as a valuable tool for image-guided interventional procedures as well as providing diagnostic information before, during, and after a procedure [13]–[17]. In particular, strain and elasticity imaging may enable noninvasive mechanical characterization of arteries and vascular pathologies [18]–[32]. Tissue displacements can be accurately measured with speckle tracking algorithms by imaging from inside a balloon catheter as a deformation is applied to the artery or lesion. Displacement data are accumulated and processed to create strain and elasticity images of vascular tissues and pathologies.

Initial studies used a noncompliant angioplasty balloon for intravascular elasticity imaging [18]–[21]. The balloon only applied a small deformation beyond its nominal inflated diameter. Due to the small deformation, strain images with good signal-to-noise ratio (SNR) are spatially limited to the balloon-tissue interface. Using a compliant silicone balloon catheter, however, the balloon can expand over a larger diameter range, producing larger internal deformations. Thus, strain images can include tissues beyond the intimal region of a vessel.

Although intravascular elasticity imaging shows promise for coronary artery diagnosis, it is particularly attractive for guiding mechanical interventions such as angioplasty and stent deployment procedures. In addition to assessing and evaluating the region of interest before and after therapy, real-time guidance and monitoring can aid clinicians in minimizing arterial damage and reducing subsequent restenosis.

A larger inflation range also can have significant clinical ramifications because several, different-sized balloon catheters are currently used to deploy stents in various sized lumens. Typically, balloons are sized in 0.5 mm diameter increments and require the clinician to accurately estimate the lumen diameter using angiography alone. A single compliant or semicompliant balloon applicable to all stenting procedures over a wide diameter range is possible if large internal deformations can be imaged and controlled accurately during deployment.

Currently, stent deployment is guided by angiography. Jomed (Rancho Cordova, CA) has developed the Josonics catheter, an initial integrated imaging/therapy device that uses intravascular ultrasound to evaluate the results of the applied therapy in vivo. However, the Josonics catheter images a plane behind the balloon instead of imaging from inside the balloon catheter at the location of the applied intravascular therapy. The goal of a fully integrated device would be to monitor deformations and elastic properties during a procedure such as stent deployment in addition to serving as a diagnostic device for pre- and post-therapy evaluation. Ultimately, the goal of guiding interventional procedures is to achieve optimal deformations with minimal injury to the artery. Real-time monitoring of the procedure could potentially reduce the percentage of restenosis by minimizing endothelial damage resulting from over inflation. Furthermore, development of an integrated imaging balloon catheter device also would reduce multiple-sized balloon catheters further as real-time quantitative feedback would result in more controlled procedures. In this study, large deformation elasticity imaging with an integrated compliant balloon ultrasound catheter

Manuscript received January 18, 2002; accepted July 26, 2002. This work was funded by NIH Grant #HL47401 and Pfizer.

C. D. Choi, S. Y. Emelianov, and M. O'Donnell are with the Department of Biomedical Engineering, University of Michigan, Ann Arbor, MI 48109-2125 (e-mail: odonnel@eecs.umich.edu).

S. Y. Emilianov recently moved to the Department of Biomedical Engineering, University of Texas, Austin, TX.

A. R. Skovoroda is with the Institute of Mathematical Problems in Biology, Russian Academy of Sciences, Pushchino, Russia.

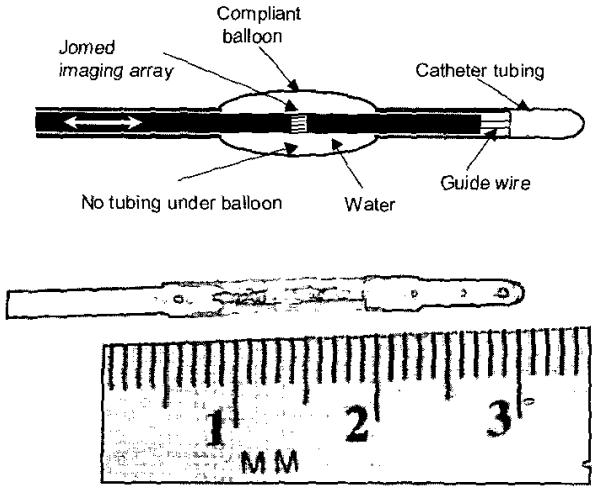

Fig. 1. Integrated compliant balloon ultrasound catheter diagram (top) and photo (bottom).

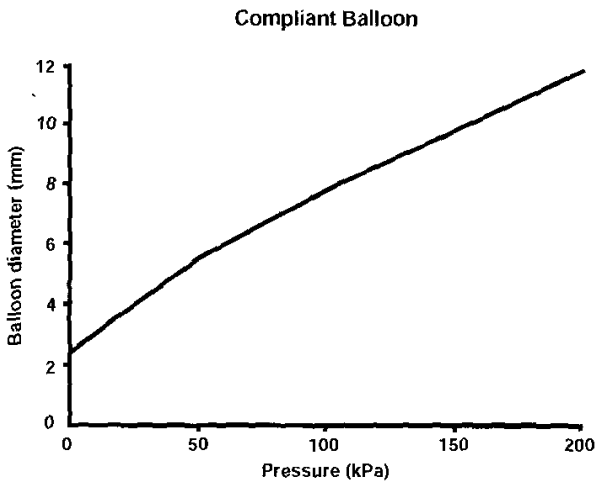

Fig. 2. Compliant balloon diameter versus pressure over a pressure range of 0–200 kPa (0–2 *atm*).

is tested on both tissue equivalent phantoms and ex vivo arterial segments.

II. Methods

Fig. 1 shows a drawing and a photograph of the integrated compliant silicone balloon catheter. It was designed in our laboratory and fabricated by Cook Veterinary Products (Bloomington, IN). The catheter diameter is 2.0 mm (6 F) with a balloon length of 10 mm. The maximum diameter of an unconstrained balloon is 12 mm. The inner lumen is large enough to house a 1.2 mm diameter (3.6 F) 64-element Jomed intravascular imaging array catheter along the center of the lumen. The lumen inner diameter is 1.6 mm and large enough to allow fluid flow around the imaging array to inflate the balloon. A guide wire is embedded into the tip of the balloon catheter and runs down the center of the lumen. It allows for easy positioning of the imaging array by sliding it over the guide wire and for collecting cross-sectional ultrasound images at different positions along the balloon length. The circumferential Jomed array operating at a center frequency of 20 MHz was used for all studies. The data acquisition system sampled beamformed RF data at 100 MHz.

Fig. 2 presents the balloon diameter as a function of intracatheter pressure for the unloaded balloon. The balloon is very compliant, producing a large increase in balloon diameter over the pressure range of 50 to 200 kPa (0.5–2.0 atm). In contrast, a noncompliant balloon changes balloon diameter by about 0.5 mm over a 1 MPa (10 atm) range after it opens to its initial diameter. Clearly, the compliant balloon can produce significant deformations over a wide range of mechanical loads.

Frames of RF data were captured in real-time at 30 frames/second during deformation. Two-dimensional speckle tracking using phase-sensitive, correlation-based techniques was performed on these data to create displacement images between frames. Differential displacement images were compensated to each frame's geometric center and accumulated over all frames in the coordinates of the geometric center of the initial frame to produce a total displacement image. All strain images are displayed in the geometry of the initial frame of the specific deformation experiment. Spatial derivatives of the displacement image produced strain images. A summary of different deformational systems and processing methods is outlined in [32]. The techniques used to process the data presented here were based on the methods described in [33]–[39].

Initial experiments were performed on a tissue-equivalent rubber phantom with controlled mechanical properties and ex vivo arterial segments, including soft (thrombus) and hard (fibrotic plaque) constituents.

A. Hard-soft Rubber Phantom

The rubber phantom was fabricated using a hardener and softener mixed with 9 μm diameter extra fine graphite scatterers. The phantom dimensions were 40 mm × 50 mm in cross section with a height of 70 mm. A 4-mm diameter hole for the integrated balloon catheter was produced in the center of the phantom spanning its height. The left half was designed to be between three and four times softer than the right half; 800 mL of hardener (#3228H, M-F Manufacturing, Fort Worth, TX) was mixed with 200 mL of softener (#4228S, M-F Manufacturing). The mixture was stirred and heated on a hot plate until clear. Then, 3 g of extra fine graphite particles were added as scatterers. The mixture was desiccated and poured into half of the rectangular mold as the hard material. As the rubber cooled, a 4-mm diameter copper rod was placed along the center axis of the mold. Then a mixture of 500 mL hardener and 500 mL softener was mixed in a beaker. The mixture was stirred and heated on a hot plate until clear.

Then, 3 g of extra fine graphite particles were added as scatterers. The mixture was desiccated and poured into the mold as the soft material. During the experiment, the catheter was placed inside the center of the phantom and pressurized up to 200 kPa (2 atm). The Young's modulus of the hard and soft materials was measured with the mechanical deformation system described in [40] and determined to be 114.8 kPa and 29.9 kPa, respectively.

A finite element simulation was designed and executed to model the phantom using the ABAQUS™ (Hibbitt, Karlsson & Sorensen, Inc., Pawtucket, RI) finite element modeling software package. The hard half was set to be 3.8 times the Young's modulus of the soft half, matching the experimentally determined ratio for the phantom. A mechanically isotropic, linear model was used for the simulation. Incompressibility and a plane strain state also were assumed. Because the strains computed from the ultrasound data had a radial depth of about 1 mm, the simulation modeled the phantom over a radius of 10 mm from the lumen center. The deformation source applied by the balloon was modeled as a uniform radial pressure of 200 kPa (2 atm) at the inner boundary (lumen) of the phantom. The outer radial boundary in the simulation was left unconstrained.

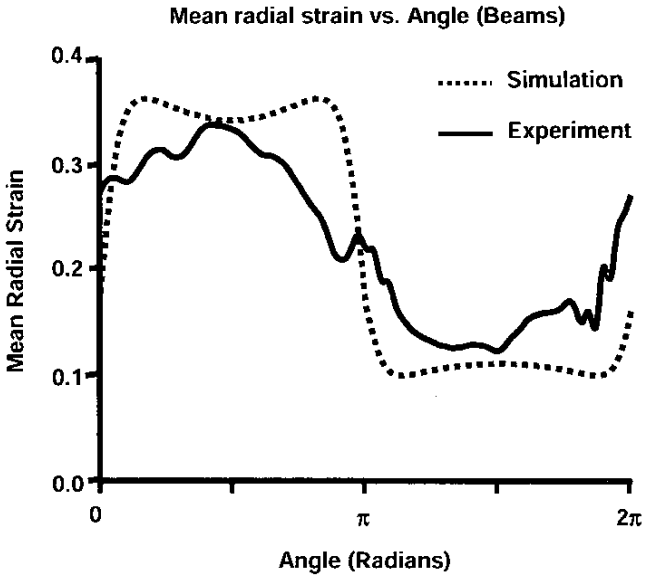

Fig. 3. Mean radial strain versus angle (beams). The hard-soft rubber phantom experiment (solid line) and the finite element simulation (dashed line) of the same object are both plotted. Radial strains were averaged over the range of 2.5 mm to 3.3 mm and plotted versus azimuth.

B. Thrombus in a Rabbit Aorta

The integrated compliant balloon ultrasound catheter was placed inside a rabbit thoracic aorta at the end of an in vivo experiment. The specific in vivo experiment was beyond the scope of this study, but consisted of applying deformations inside the rabbit thoracic aorta with the integrated compliant balloon ultrasound catheter. A small incision was made near the femoral artery for the catheter to enter the aorta. The balloon was inflated up to 200 kPa (2 atm). When the in vivo experiment concluded, the animal was euthanized, and the catheter remained in the thoracic aorta for 1 hour as a thrombus developed inside the vessel. Then, a 2-cm segment of rabbit thoracic aorta containing the thrombus and the integrated compliant balloon ultrasound catheter was excised. The artery was clamped to the catheter at the proximal and distal ends of the balloon with sutures. Then, the catheter with the thrombus and artery was placed in a small water tank filled with deionized and degassed water. For this study, an ex vivo experiment was chosen to clearly verify that the imaging plane included the thrombus and to track displacements without superimposed respiratory motion. The balloon was pressurized up to 200 kPa (2 atm) during the deformation experiment. Following this experiment, the artery was dissected and the clot position was confirmed.

C. Fibrotic Human Plaque Ex Vivo

A 4-cm long segment of human left femoral artery containing fibrotic lesions was obtained at autopsy from a 60-year-old male. To approximate the mechanical environment in vivo, the artery segment was embedded in a gelatin mold, including 9-μm diameter graphite scatterers. A 450 mL volume of water was mixed with 25 g of gelatin. Then, 1.3 g of extra fine graphite particles was added as scatterers. The gelatin was measured to have a Young's modulus of 18.25 kPa using the mechanical deformation system. The balloon catheter was placed inside the artery and pressurized to 200 kPa (2 atm). Following deformation studies, the artery was dissected and lesions were identified by palpation. Each side of the phantom was marked and referenced with the array catheter position in the phantom. After the experiment, plaque position in the ultrasound data was matched with the excised plaque position for confirmation.

III. Results

A. Hard-soft Rubber Phantom

Displacement data were accumulated over 86 frames. Average radial normal strain in the hard rubber region was 12% compared to 33.5% for the soft region. In Figs. 3 and 4, experimental results are compared to a finite element simulation using the same geometry and assuming the right half of the phantom is a factor of 3.8 times harder than the left half. In Fig. 3, radial strains were averaged over the range of 2.5 mm to 3.3 mm for both cases and plotted versus angle (beam direction). In Fig. 4 radial strains were averaged over 0.078 radians (20 beams) at the middle of the soft region and plotted versus depth. In both cases, experimental results vary from simulations but follow the general trend of the simulations. In Fig. 3, the smoothing effect of the radial strain measurements at the transition

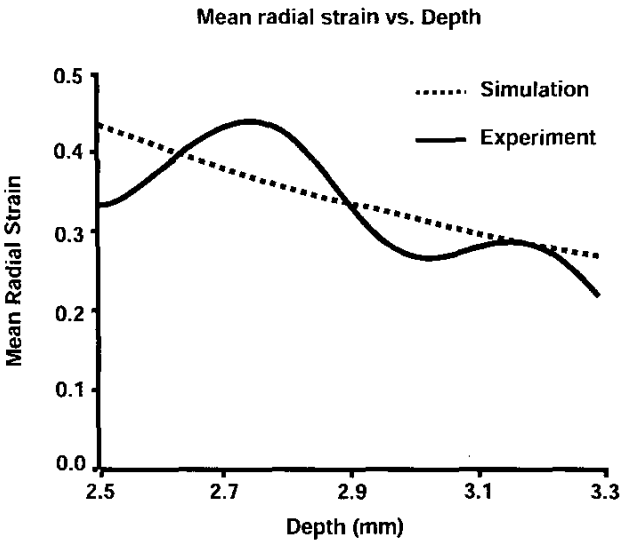

Fig. 4. Mean radial strain versus depth. The hard-soft rubber phantom experiment (solid line) and the finite element simulation (dashed line) of the same object are compared in the soft region of the phantom. Radial strains were averaged over ± 10 beams at the angle (beam) of highest strain (angle $= \pi/2$ radians as shown in Fig. 3).

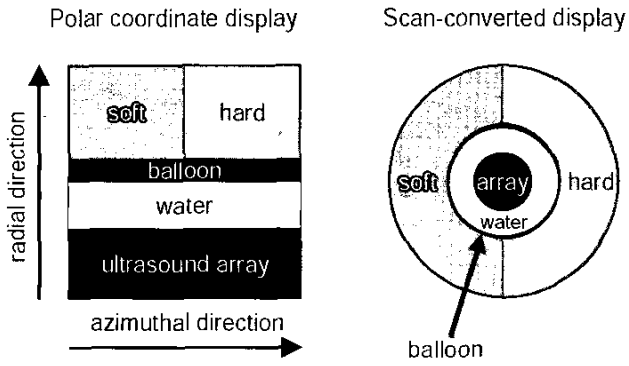

Fig. 5. On the left, the polar coordinate (r-theta) is displayed; on the right the scan-converted display for the hard-soft rubber phantom is shown. The catheter array is at the bottom of the polar coordinate display and at the center of the scan-converted display.

regions between the hard and soft materials can be attributed to the larger shear strains in these regions and the influence of the balloon-tissue interface. In Fig. 4, radial strain variations could be due to small inhomogeneities in the phantom due to the rubber mixing with graphite scatterers or noise from speckle tracking algorithms that are sensitive to local variations in SNR and strain.

Fig. 5 illustrates the polar (left) and scan-converted (right) display formats. For the hard-soft rubber phantom, the polar display emphasizes the radial dependence of the strain pattern, and the scan-converted display presents the true geometry. In Figs. 6 and 7, images are shown for the hard-soft rubber phantom experiment (Fig. 6) and finite element simulation (Fig. 7) in polar coordinates with the catheter located at the bottom of the image, and the range direction increasing along the vertical axis. The horizontal axis refers to azimuth, or beam direction. The left image is the B scan presented over a 40 dB display dynamic range. The middle panel is a grayscale radial strain image displayed over a range of 15% to 40%. The right image is the B scan from the left image superimposed with a color strain image. In both Figs. 6 and 7, the right image is displayed using a "hot" color map to emphasize softer regions. Strains higher than 40% are shown in yellow and strains lower than 22% are not shown. Images are presented over a range of 2.5 mm to 3.3 mm from the catheter center. The range direction was interpolated three times to better illustrate radial variations in the strain images.

Figures 8 and 9 are the corresponding images to Figs. 6 and 7, respectively, shown in the scan-converted display. The dimensions of all images in Figs. 8 and 9 are 7 mm $\times$ 7 mm.

B. Thrombus in a Rabbit Aorta

Displacement data were accumulated over 36 frames. Fig. 10 contains both a B scan (left) of the rabbit thoracic aorta, a grayscale strain image (middle) displayed over a range of 0 to 35%, and a strain image superimposed on the B scan (right) with strain values displayed from 10–35%. Strains greater than 35% are in bright red; those less than 10% are not displayed. The total display is 8 mm $\times$ 8 mm for each image. The soft clot and the arterial wall are clearly visible in the combined B scan/strain image. The presence and location of a thrombus were verified after the deformation experiment.

C. Fibrotic Human Plaque Ex Vivo

Displacements were accumulated over 57 frames. Fig. 11 contains a B scan of the femoral artery (left), an inverted grayscale radial strain image (middle) displayed over a 0 (white) to 20% (black) range, and the B scan with the superimposed strain image (right) with strains ranging from 7% to 20% presented in color (cool scale). The largest fibrotic plaque is located between 2 o'clock and 3 o'clock in the images. This region is hyperechoic in the B scan and suggests some calcification. The strain dynamic range in the right image is from 7–20% to highlight harder regions of the artery. Thus, strains less than 7% are shown in bright pink; those greater than 20% are not shown. In addition to the calcified plaque, two other low strain regions are located at 8 o'clock and 12 o'clock in the strain image that are not visible in the B scan alone. The total display is 7.2 mm $\times$ 7.2 mm for each image. The locations of the fibrotic lesions were confirmed by manual palpation at dissection after the deformation experiment.

IV. Discussion

Strain images for a hard-soft phantom, thrombus, and fibrotic human plaque illustrate large strains applied by the integrated compliant balloon ultrasound catheter. Al-

Fig. 6. Hard-soft rubber phantom shown in r (vertical)-theta (horizontal) display format interpolated three times in the radial direction. Images are displayed over a range of 2.5 mm to 3.3 mm. Left panel contains a B scan displayed over 40 dB. Middle panel contains a grayscale strain image displayed over a range of 15-40%. The right panel contains the B scan from the left panel superimposed by the strain image displayed in color (hot scale) over a strain range of 22-40%.

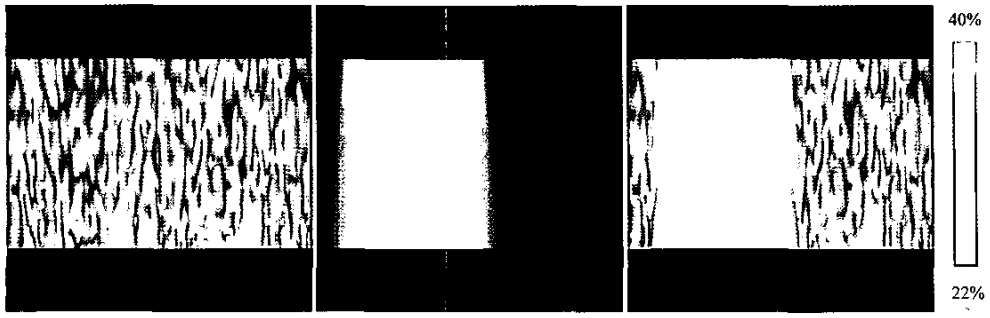

Fig. 7. Finite-element simulation results of hard-soft rubber phantom are shown in the same polar format and ranges as those in the corresponding panels in Fig. 6.

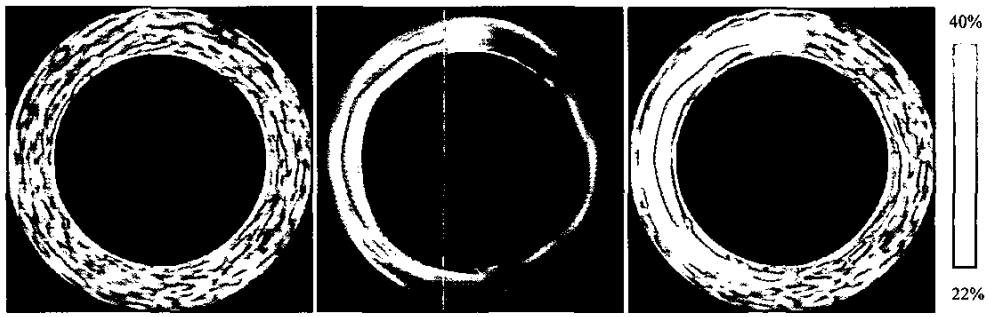

Fig. 8. Hard-soft rubber phantom (scan-converted images of the data shown in Fig. 6). Dimensions of each panel are 7 mm × 7 mm.

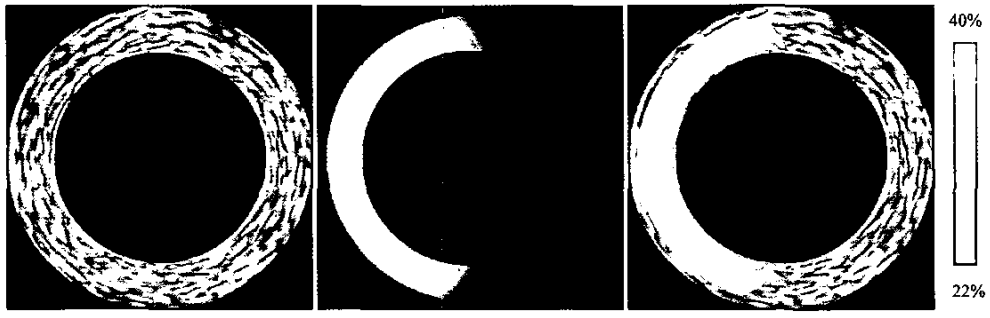

Fig. 9. Finite-element simulation of hard-soft rubber phantom (scan-converted images of the data shown in Fig. 7). Dimensions of each panel are 7 mm × 7 mm.

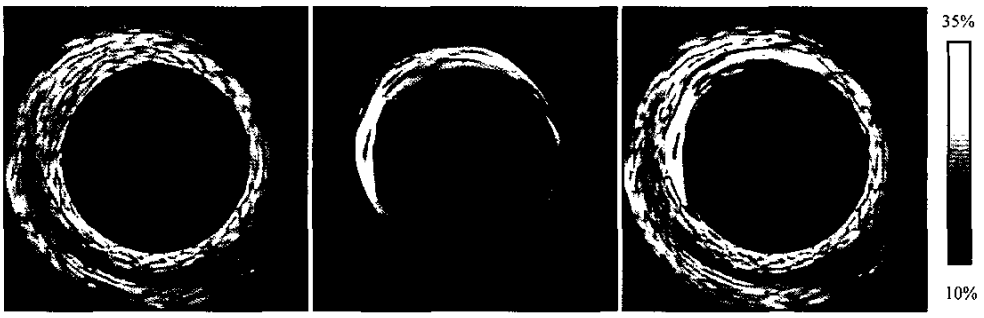

Fig. 10. Thrombosis in excised rabbit thoracic aorta. Left panel contains a B scan displayed over 40 dB. Middle panel contains a grayscale strain image displayed over a range of 0–35%. The right panel contains the B scan from the left panel superimposed by the strain image displayed in color (red scale) over a strain range of 10–35%. Dimensions of each panel are 8 mm × 8 mm.

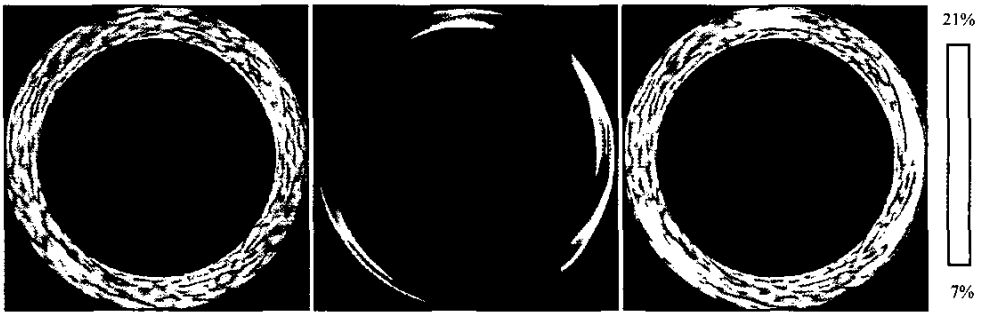

Fig. 11. Fibrotic plaque in human femoral artery. Left panel contains a B scan displayed over 40 dB. Middle panel contains a grayscale strain image displayed over a range of 0–20%. The right panel contains the B scan from the left panel superimposed by the strain image displayed in color (cool scale) over a strain range of 7–20%. Dimensions of each panel are 7.2 mm × 7.2 mm.

though the phantom experiment contained noise from speckle tracking and possible local inhomogeneities in the phantom, the rubber hard-soft phantom experiment results agreed reasonably well with finite element simulations. In addition, ex vivo experiments with two vascular pathologies were performed to measure strains in soft (rabbit thrombus) and hard (fibrotic human plaque) tissues. The ex vivo results suggest that the integrated compliant balloon ultrasound catheter can apply and measure strains for these two cases with vastly different mechanical properties. The more challenging cases of vulnerable plaques and highly heterogeneous pathologies need to be examined using this catheter.

For all deformation experiments, the balloon was never pressurized by more than 200 kPa (2 atm). Strains can easily be imaged over about 1 mm of radial depth in each case and, consequently, compliant balloon deformations produce greater spatial extent, high SNR strain images. In contrast to the compliant balloon results presented here, past experiments using a noncompliant balloon with the same Jomed catheter imaging system involved pressures of 800 kPa (8 atm), deformations resulting in 1–4% strains, and a radial extent of only about 200 μm in strain images [18]–[20].

The integrated compliant balloon ultrasound catheter using a Jomed intravascular ultrasound array could potentially guide stent deployment to minimize endothelial damage and subsequent restenosis [41]. The compliant or semicompliant balloon will enable a single-sized balloon catheter for stent deployment, producing large tissue deformations at lower pressures. Furthermore, real-time pressure and cross-sectional area recordings could quantitatively determine full stent deployment with this system [21]. This catheter also could provide mechanical information about tissues while guiding angioplasty procedures. The results presented here suggest that high strains associated with mechanical interventions such as angioplasty and stent deployment can be measured with the integrated imaging balloon catheter.

Although strain images suggest contrast in material properties for the cases presented here, elasticity reconstruction may still be required to determine relative Young's modulus values from these experiments. Furthermore, results need to be compared to both histological and biochemical measurements assessing tissue damage and correlated with elasticity images.

It is important to note the size of the integrated compliant balloon ultrasound catheter used in these experiments. Although adequate for peripheral vascular studies, a diameter of 2 mm (6 F) is large for many other vascular applications. This catheter is meant to serve as a test vehicle for future studies. The catheter will be miniaturized for clinical experiments with the intention of moving toward coronary interventions.

Due to the lower pressure, arterial remodeling could be minimized even at the high measured strains because tissue regions experiencing larger deformations are presumably very soft. Further histological and in vivo studies must be conducted to verify this hypothesis.

Several other issues need to be resolved before an integrated imaging balloon catheter device can be used clinically. Currently, the guide wire is embedded into the tip of the catheter. For coronary applications, the guide wire must have its own port within the balloon catheter for conventional positioning. This could be placed in the tip of an integrated balloon ultrasound catheter. In addition to the guide wire, other balloon materials will be tested to ensure the integrated catheter applies adequate arterial tissue deformations for angioplasty and stent deployment procedures.

Ultimately, an integrated imaging balloon ultrasound catheter would serve as a multifunctional diagnostic and therapeutic guidance device for all intravascular interventions. Preprocedure, the imaging array could help guide the positioning of the balloon catheter as well as acquiring information about the structure, morphology, and flow in the region of interest. Then, real-time monitoring during the procedure would aid clinicians in performing optimal interventional procedures resulting in minimal damage to the arterial wall. Additionally, elastic properties of the pathology and/or vessel could be acquired during the deformation. Postprocedure, the same information taken prior to the applied therapy could be taken to compare with preprocedure conditions. Measuring the structure, morphology, and flow in the vessel would allow for rapid assessment of the therapy's outcome. By providing not only diagnostic information but also therapeutic guidance to angioplasty and stent deployment, an integrated imaging balloon catheter could reduce restenosis rates and provide quantitative means for determining optimal interventional procedures.

Acknowledgments

The authors would like to thank Jomed, Inc., for their continued support of this work through both their equipment and cooperation. We also would like to thank Dr. Mark Rekhter and Dr. Mike Ryan at Pfizer Global Research and Development for their support and biological expertise. We also are grateful to Dr. John Crowe and Dr. Mark Lubinski for developing software tools to process the data efficiently, and to Ramon Erkamp for building the mechanical deformation system. We would also like to thank Mr. Jeffery Catlin for his collaboration and assistance in fabricating the balloon catheters.

References

[1] American Heart Association, *2001 Heart and Stroke Statistical Update*. Dallas, TX: American Heart Association, 2000, pp. 29–30.

[2] H. M. Loree, R. D. Kamm, R. G. Stringfellow, and R. T. Lee, "Effects of fibrous cap thickness on peak circumferential stress in model atherosclerotic vessels," *Circul. Res.*, vol. 71, pp. 850–858, 1992.

[3] H. M. Loree, A. J. Grodzinsky, S. Y. Park, L. J. Gibson, and R. T. Lee, "Static circumferential tangential modulus of human atherosclerotic tissue," *J. Biomechan.*, vol. 27, pp. 195–204, 1994.

[4] F. A. Duck, *Physical Properties of Tissue*. San Diego, CA: Academic, 1990.

[5] M. D. Rekhter, G. W. Hicks, D. W. Brammer, C. W. Work, J. Kim, D. Gordon, J. A. Keiser, and M. J. Ryan, "Animal model that mimics atherosclerotic plaque rupture," *Circul. Res.*, vol. 83, pp. 705–713, 1998.

[6] E. Falk, "Why do plaques rupture?," *Circulation*, vol. 86, Suppl. III, pp. III-30–III-42, 1992.

[7] R. T. Lee and P. Libby, "The unstable atheroma," *Atheroscler. Thromb. Vasc. Biol.*, vol. 17, pp. 1859–1867, 1997.

[8] P. Libby, "Molecular bases of acute coronary syndromes," *Circulation*, vol. 91, pp. 2844–2850, 1995.

[9] Y. Uchida, F. Nakamura, T. Tomaru, T. Morita, T. Oshima, T. Sasaki, S. Morizuki, and J. Hirose, "Prediction of acute coronary syndromes by percutaneous coronary angioscopy in patients with stable angina," *Amer. Heart J.*, vol. 130, pp. 195–203, 1995.

[10] R. T. Lee, F. J. Schoen, H. M. Loree, M. W. Lark, and P. Libby, "Circumferential stress and matrix metalloproteinasel in human coronary atherosclerosis: Implications of plaque rupture," *Arterioscler. Thromb. Vasc. Biol.*, vol. 16, pp. 1070–1073, 1996.

[11] R. T. Lee, A. J. Grodzinsky, E. H. Frank, R. D. Kamm, and F. J. Schoen, "Structure-dependent dynamic mechanical behavior of fibrous caps from human atherosclerotic plaques," *Circulation*, vol. 83, pp. 1764–1770, 1991.

[12] A. Farb, A. P. Burke, A. L. Tang, Y. Liang, P. Mannan, J. Smialek, and R. Virmani, "Coronary plaque erosion without rupture into a lipid core," *Circulation*, vol. 93, pp. 1354–1363, 1996.

[13] C. R. Meyer, E. H. Chang, K. P. Fechner, D. W. Fitting, D. M. Williams, and A. J. Buda, "Feasibility of high-resolution intravascular ultrasonic imaging catheters," *Radiology*, vol. 168, pp. 113–116, 1988.

[14] N. F. Starksen and P. G. Yock, "Clinical applications of intravascular ultrasound imaging," *Amer. J. Cardiac Imaging*, vol. 5, pp. 54–59, 1991.

[15] M. O'Donnell, B. M. Shapo, M. J. Eberle, and D. N. Stephens, "Experimental studies on an efficient catheter array imaging system," *Ultrason. Imag.*, vol. 17, pp. 83–94, 1995.

[16] M. O'Donnell and L. J. Thomas, "Efficient synthetic aperture imaging from a circular aperture with possible application to catheter-based imaging," *IEEE Trans. Ultrason., Ferroelect., Freq. Contr.*, vol. 39, pp. 366–380, 1992.

[17] M. O'Donnell, M. J. Eberle, D. N. Stephens, J. L. Litzza, K. San Vincente, and B. M. Shapo, "Synthetic phased arrays for intraluminal imaging of coronary arteries," *IEEE Trans. Ultrason., Ferroelect., Freq. Contr.*, vol. 44, pp. 714–717, 1997.

[18] B. M. Shapo, J. R. Crowe, A. R. Skovoroda, M. J. Eberle, N. A. Cohn, and M. O'Donnell, "Displacement and strain imaging of coronary arteries with intraluminal ultrasound," *IEEE Trans. Ultrason., Ferroelect., Freq. Contr.*, vol. 43, pp. 234–246, 1996.

[19] B. M. Shapo, J. R. Crowe, R. Q. Erkamp, S. Y. Emelianov, M. J. Eberle, and M. O'Donnell, "Strain imaging of coronary arteries with intraluminal ultrasound: Preliminary experimental results," in *Proc. IEEE Ultrason. Symp.*, 1996, pp. 1177–1180.

[20] B. M. Shapo, J. R. Crowe, S. Y. Emelianov, M. J. Eberle, and M. O'Donnell, "Strain imaging of coronary arteries with intraluminal ultrasound: Experiments on an inhomogeneous phantom," *Ultrason. Imag.*, vol. 18, pp. 173–191, 1996.

[21] M. O'Donnell, M. J. Eberle, D. N. Stephens, J. L. Litzza, B. M. Shapo, J. R. Crowe, C. D. Choi, J. J. Chen, D. W. M Muller, J. A. Kovach, R. L. Lederman, R. C. Ziegenbein, C. C. Wu, K. San Vicente, and D. Bleam, "Catheter arrays: Can intravascular ultrasound make a difference in managing coronary artery disease?," in *Proc. IEEE Ultrason. Symp.*, 1997, pp. 1447–1456.

[22] L. K. Ryan and F. S. Foster, "Ultrasonic measurement of differential displacement and strain in a vascular model," *Ultrason. Imag.*, vol. 19, pp. 19–38, 1997.

[23] C. L. de Korte, S. G. Carlier, F. Mastik, A. F. W. van der Steen, E. I. Cespedes, P. W. Serruys, and N. Bom, "Intracoronary elastography in the catheterization laboratory: Preliminary patient results," in *Proc. IEEE Ultrason. Symp.*, 1999, pp. 1649–1652.

[24] C. L. de Korte, E. I. Cespedes, A. F. W. van der Steen, B. Norder, and K. te Nijenhuis, "Elastic and acoustic properties

of vessel mimicking material for elasticity imaging," *Ultrason. Imag.*, vol. 19, pp. 112–126, 1997.
[25] L. K. Ryan and F. S. Foster, "Ultrasonic measurement of differential displacement and strain in a vascular model," *Ultrason. Imag.*, vol. 19, pp. 19–28, 1997.
[26] C. L. de Korte, E. I. Cespedes, A. F. W. van der Steen, and C. T. Lancee, "Intravascular elasticity imaging using ultrasound: Feasibility studies in phantoms," *Ultrasound Med. Biol.*, vol. 23, pp. 735–746, 1997.
[27] C. L. de Korte, A. F. W. van der Steen, E. I. Cespedes, and G. Pasterkamp, "Intravascular ultrasound elastography in human arteries: Initial experience in vivo," *Ultrasound Med. Biol.*, vol. 24, pp. 401–408, 1998.
[28] L. K. Ryan and F. S. Foster, "Tissue equivalent vessel phantoms for intravascular ultrasound," *Ultrasound Med. Biol.*, vol. 23, pp. 261–273, 1997.
[29] R. J. Siegel, M. Ariani, M. C. Fishbein, J. Chae, J. C. Park, G. Maurer, and J. S. Forrester, "Histopathologic validation of angioscopy and intravascular ultrasound," *Circulation*, vol. 84, pp. 109–117, 1991.
[30] J. A. Mallery, J. M. Tobis, J. Griffith, J. Gessert, M. McRae, O. Moussabeck, M. Bessen, M. Moriuchi, and W. L. Henry, "Assessment of normal and atherosclerotic arterial wall thickness with an intravascular ultrasound imaging catheter," *Amer. Heart J.*, vol. 119, pp. 1392–1400, 1990.
[31] R. T. Lee, G. Richardson, H. M. Loree, A. J. Grodzinsky, S. A. Gharib, F. J. Schoen, and N. Pandian, "Prediction of mechanical properties of human atherosclerotic tissue by high-frequency intravascular ultrasound imaging," *Arterioscler. Thromb.*, vol. 12, pp. 1–5, 1992.
[32] E. I. Cespedes, C. L. de Korte, and A. F. W. van der Steen, "Intraluminal ultrasonic palpation: Assessment of local and cross-sectional tissue stiffness," *Ultrasound Med. Biol.*, vol. 26, pp. 285–296, 2000.
[33] S. Y. Emelianov, M. A. Lubinski, W. F. Weitzel, R. C. Wiggins, A. R. Skovoroda, and M. O'Donnell, "Elasticity imaging for early detection of renal pathology," *Ultrasound Med. Biol.*, vol. 21, pp. 871–883, 1995.
[34] M. A. Lubinski, S. Y. Emelianov, and M. O'Donnell, "Speckle tracking methods for ultrasonic elasticity imaging using short-time correlation," *IEEE Trans. Ultrason., Ferroelect., Freq. Contr.*, vol. 46, pp. 82–96, 1999.
[35] A. R. Skovoroda, S. Y. Emelianov, M. A. Lubinski, A. P. Sarvazyan, and M. O'Donnell, "Theoretical analysis and verification of ultrasound displacement and strain imaging," *IEEE Trans. Ultrason., Ferroelect., Freq. Contr.*, vol. 41, pp. 302–313, 1994.
[36] M. O'Donnell, A. R. Skovoroda, B. M. Shapo, and S. Y. Emelianov, "Internal displacement and strain imaging using ultrasonic speckle tracking," *IEEE Trans. Ultrason., Ferroelect., Freq. Contr.*, vol. 41, pp. 314–325, 1994.
[37] N. A. Cohn, S. Y. Emelianov, M. A. Lubinski, and M. O'Donnell, "An elasticity microscope. Part I: Methods," *IEEE Trans. Ultrason., Ferroelect., Freq. Contr.*, vol. 44, pp. 1304–1319, 1997.
[38] N. A. Cohn, S. Y. Emelianov, M. A. Lubinski, and M. O'Donnell, "An elasticity microscope. Part II: Experimental results," *IEEE Trans. Ultrason., Ferroelect., Freq. Contr.*, vol. 44, pp. 1320–1331, 1997.
[39] M. A. Lubinski, S. Y. Emelianov, and M. O'Donnell, "Adaptive strain estimation using retrospective processing," *IEEE Trans. Ultrason., Ferroelect., Freq. Contr.*, vol. 46, pp. 97–107, 1999.
[40] R. Q. Erkamp, P. Wiggins, A. R. Skovoroda, S. Y. Emelianov, and M. O'Donnell, "Measuring the elastic modulus of small tissue samples," *Ultrason. Imag.*, vol. 20, pp. 17–28, 1998.
[41] A. Columbo, P. Hall, S. Nakamura, Y. Almagor, L. Maiello, G. Martini, A. Gaglione, S. L. Goldberg, and J. M. Tobis, "Intracoronary stenting without anticoagulation accomplished with intravascular ultrasound guidance," *Circulation*, vol. 91, pp. 1676–1688, 1995.

Charles D. Choi (S'93) received the B.S.E. in electrical and biomedical engineering from Duke University, Durham, NC, in 1995. He received an M.S. in biomedical engineering in 1997 and an M.S.E. in electrical engineering and computer science in 1998 both at the University of Michigan, Ann Arbor, MI. He is currently a Ph.D. candidate at the University of Michigan working with Dr. Matthew O'Donnell in the Biomedical Ultrasonics Lab.

His research focuses on using intravascular ultrasound to measure mechanical properties of arterial tissues and pathologies and to develop an integrated balloon ultrasound catheter to guide interventional procedures such as angioplasty and stent deployment.

Andrei R. Skovoroda received the B.S. and M.S. degrees in mathematics and mechanics in 1973 and 1974, respectively, from the Novosibirsk State University, and the Ph.D. degree in 1985 from the Moscow State University. From 1975 to 1977 he was a lecturer in theoretical mechanics at the College of Textile Technology, Barnaul, Russia. From 1977 to 1980 he was a Ph.D. researcher at the subfaculty of Plasticity of the Moscow State University, where he worked on the dynamic behavior of plates under blast-type loading. In 1981 he held an appointment as a junior research associate at the Laboratory of Mathematical Modeling of the Research Computing Center, Pushchino, Russia, of the USSR Academy of Sciences (the present name is the Institute of Mathematical Problems in Biology, Russian Academy of Sciences), where he developed efficient mathematical methods to solve the differential equations of the theory of elasticity. In 1986 he became a senior research associate and was Scientific Secretary at the same Institute from 1988 to 1993. He is currently the Head of the Laboratory of Mathematical Problems in Biomechanics and works on the biomechanics of soft tissue.

Dr. Skovoroda has authored and co-authored over 110 articles for archival publications and papers that were presented at All-Union and International meetings.

Stanislav Emelianov (M'94) was born in May 1966. He received the B.S. and M.S. degrees in physics in 1986 and 1989, respectively, from the Moscow State University, and the Ph.D. degree in physics in 1993 from Moscow State University, and the Institute of Mathematical Problems of Biology, Pushchino, Russia, of the Russian Academy of Sciences, Russia.

In 1989, he joined the Institute of Mathematical Problems of Biology, where he was engaged in both mathematical modeling of soft tissue biomechanics and experimental studies of noninvasive methods in medical diagnostics based on tissue elasticity variations.

Following his graduate work, Dr. Emelianov moved to the University of Michigan, Ann Arbor, as a postdoctoral fellow in the Bioengineering Program, and Electrical Engineering and Computer Science Department. From 1996 to 2002, Dr. Emelianov was a Research Scientist at the Biomedical Ultrasonics Laboratory at the University of Michigan. During his tenure at Michigan, Dr. Emelianov was involved primarily in the theoretical and practical aspects of elasticity imaging. He is currently an Assistant Professor of Biomedical Engineering at the University of Texas, Austin. His research interests are in the areas of diagnostic ultrasound, medical imaging systems, tissue biomechanics, and nondestructive material testing.

Matthew O'Donnell (M'79-SM'84-F'93) received his B.S. and Ph.D. degrees in physics from the University of Notre Dame, Notre Dame, IN, in 1972 and 1976, respectively. Following his graduate work, Dr. O'Donnell moved to Washington University in St. Louis as a postdoctoral fellow in the Physics Department working on applications of ultrasonics to medicine and nondestructive testing. He subsequently held a joint appointment as a senior research associate in the Physics Department and a research instructor of Medicine in the Department of Medicine at Washington University. In 1980 he moved to General Electric Corporate Research and Development Center in Schenectady, NY, where he continued to work on medical electronics, including MRI and ultrasound imaging systems. During the 1984–1985 academic year, he was a visiting fellow in the Department of Electrical Engineering at Yale University, New Haven, CT, investigating automated image analysis systems.

In a bold move during 1990, Dr. O'Donnell became a Professor of Electrical Engineering and Computer Science at the University of Michigan in Ann Arbor, MI. Since 1997, he has held a joint appointment as Professor of Biomedical Engineering at Michigan, and in 1998 he was named the Jerry W. and Carol L. Levin Professor of Engineering. Currently, he is the Chair of the Biomedical Engineering Department. Dr. O'Donnell's most recent work has explored new imaging modalities in biomedicine, including elasticity imaging, in vivo microscopy, optoacoustic arrays, optoacoustic contrast agents, and catheter-based devices.